Physics of the Earth and Planetary Interiors 177 (2009) 1–11

Contents lists available at ScienceDirect

Physics of the Earth and Planetary Interiors

journal homepage: www.elsevier.com/locate/pepi

Estimation of surface wave Green's functions from correlation of direct waves, coda waves, and ambient noise in SE Tibet

Huajian Yao[a,*], Xander Campman[b], Maarten V. de Hoop[c], Robert D. van der Hilst[a]

[a] Department of Earth, Atmospheric, and Planetary Sciences, Massachusetts Institute of Technology, Cambridge, MA 02139, USA
[b] Shell International E&P B.V., Kessler Park 1, 2288 GS, Rijswijk, The Netherlands
[c] Center for Computational and Applied Mathematics, Purdue University, West-Lafayette, USA

ARTICLE INFO

Article history:
Received 29 October 2008
Received in revised form 23 June 2009
Accepted 1 July 2009

Keywords:
Empirical Green's function
Seismic interferometry
Ambient noise
Surface waves
Coda
Beamforming

ABSTRACT

Empirical Green's functions (EGFs) between receivers can be obtained from seismic interferometry through cross-correlation of pairs of ground motion records. Full reconstruction of the Green's function requires diffuse wavefields or a uniform distribution of (noise) sources. In practice, EGFs differ from actual Green's functions because wavefields are not diffuse and the source distribution not uniform. This difference, which may depend on medium heterogeneity, complicates (stochastic) medium characterization as well as imaging and tomographic velocity analysis with EGFs. We investigate how source distribution and scale lengths of medium heterogeneity influence surface wave Green's function reconstruction in the period band of primary microseisms (T = 10–20 s). With data from a broad-band seismograph array in SE Tibet we analyze the symmetry and travel-time properties of surface wave EGFs from correlation of data in different windows: ambient noise, direct surface waves, and surface wave coda. The EGFs from these different windows show similar dispersion characteristics, which demonstrates that the Green's function can be recovered from direct wavefields (e.g., ambient noise or earthquakes) or from wavefields scattered by heterogeneity on a regional scale. Directional bias and signal-to-noise ratio of EGFs can be understood better with (plane wave) beamforming of the energy contributing to EGF construction. Beamforming also demonstrates that seasonal variations in cross-correlation functions correlate with changes in ocean activity.

1. Introduction

Traditional seismic imaging and tomographic velocity analysis of Earth's interior relies on data associated with ballistic (source–receiver) wave propagation. However, over the past few years one has also started to use information contained in seismic coda waves and ambient noise to image the Earth's structure from regional scale to continental scale (Campillo and Paul, 2003; Shapiro and Campillo, 2004; Shapiro et al., 2005; Bakulin and Calvert, 2006; Willis et al., 2006; Yao et al., 2006, 2008; Yang et al., 2007). Modal representation of diffuse wavefields, elastodynamic representation theorems, and stationary phase arguments (Weaver and Lobkis, 2004, 2005; Wapenaar, 2004, 2006; Snieder, 2004; Paul et al., 2005; Roux et al., 2005; Nakahara, 2006) have been used to argue that the Green's function between the two stations can be estimated from the summation of cross-correlations of continuous records of ground motion at these stations. These studies make different assumptions about noise (source) characteristics and (stochastic) properties of the medium. The results of ambient noise cross-correlation are analyzed by Colin de Verdière (2006a,b), Bardos et al. (2008), and De Hoop and Solna (2008).

Continuous records of ground motion typically contain seismic energy in several regimes. For example, earthquakes generate deterministic, transient energy that can be registered as distinct phase arrivals by seismometers. Non-smooth medium heterogeneity can, however, complicate waveforms in such a way that they can no longer be described deterministically. After multiple scattering the wavefield may become diffuse. This regime is often called the seismic coda, mostly arriving after the ballistic waves (see, for instance, Sato and Fehler, 1998). Outside the time windows dominated by direct and coda waves from earthquakes continuous records contain energy that is mainly due to continuous processes near and below Earth's surface. This regime is often referred to as ambient seismic noise. In theory, the cross-correlation and summation approach can be applied to each of these regimes to obtain an empirical Green's function (EGF), as long as energy arrives at the two seismic stations from all directions and in all possible modes (assuming equipartitioning).

For simple media cross-correlation of the ballistic responses due to sources surrounding two receivers gives the exact Green's func-

* Corresponding author.
E-mail address: hjyao@mit.edu (H. Yao).

0031-9201/$ – see front matter © 2009 Elsevier B.V. All rights reserved.
doi:10.1016/j.pepi.2009.07.002

tion between the receivers (De Hoop and De Hoop, 2000; Wapenaar, 2004). In practice, seismic energy is neither uniformly distributed nor equipartitioned (Malcolm et al., 2004; Sánchez-Sesma et al., 2008; Paul et al., 2005). In field experiments, equipartitioning is generally not achieved because the mode structure of the wavefield depends on the mechanism and the location of the noise sources. Moreover, equipartitioned waves are weak and their contribution to the wavefield can easily be overwhelmed by (directional) waves and noise, as shown below. As a consequence, Green's functions are not fully reconstructed, and the accuracy of reconstruction is generally unknown. How well the Green's function is estimated depends on the mechanism and spatial distribution of the noise sources as well as the properties of the medium beneath the receiver arrays. On the positive side, one could exploit this dependence to constrain (stochastic) medium properties (e.g., Scales et al., 2004) if the effects of noise distribution can be accounted for. In this context, the length scale of heterogeneity, the frequency content of the wavefields, and the spatial and temporal spectra of noise sources are all important (De Hoop and Solna, 2008). On the negative side, the (unknown) uncertainty in Green's function construction complicates imaging and, in particular, multi-scale (tomographic) velocity analysis with EGFs.

The problem of incomplete Green's function reconstruction has been recognized before – see, for instance, Yao et al. (2006) for cases of incomplete reconstruction of EGFs for Rayleigh wave propagation) – and practical solutions have been proposed. For active source applications of seismic interferometry, source distributions can be designed with the objective to optimize the retrieval of the Green's function (Metha et al., 2008). In earthquake seismology, where the source configuration cannot be manipulated, one can enhance the illumination of receiver arrays by ballistic waves either by waiting long enough for contributions from a large range of source areas to accumulate or one can make better use of the (continuously) recorded wavefield.

To improve the inference of medium properties from EGFs or the imaging or velocity analysis of complex media with EGFs we need a more comprehensive understanding of the relationships between EGFs and medium heterogeneity and properties of noise sources. De Hoop and Solna (2008) present a theoretical framework for the estimation of Green's functions in medium with random fluctua-

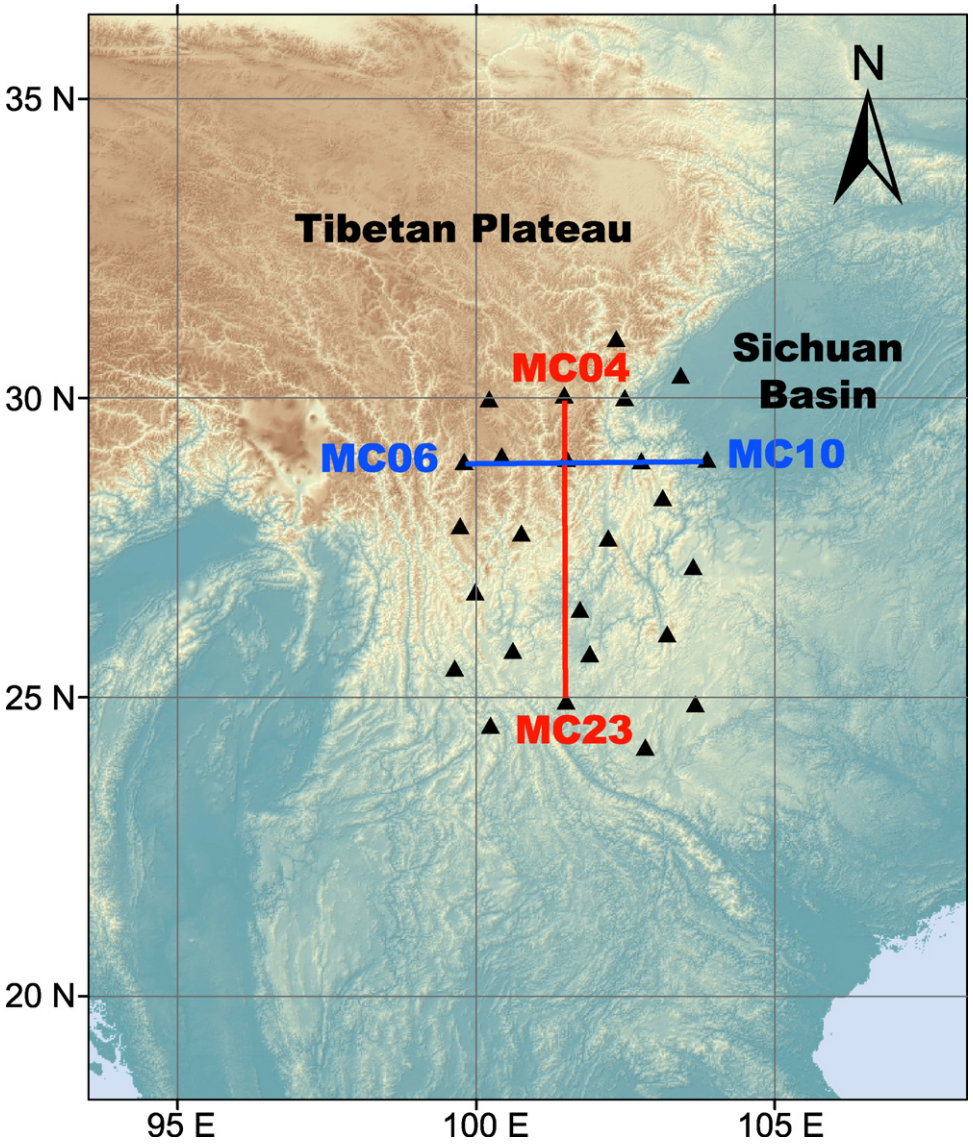

Fig. 1. The location of 25 stations (black triangles) of the MIT-CIGMR array in SE Tibet. The red line and the blue line show the two-station paths for the S–N directional station pair MC04–MC23 and the E–W directional station pair MC06–MC10, respectively. (For interpretation of the references to colour in this figure legend, the reader is referred to the web version of the article.)

tions; and show that EGFs are related to the actual Green's function through a convolution with a statistically stable filter that depends on the medium fluctuations.

Using field observations (from an array in SW China) we investigate here the different contributions of the wavefield to the construction of EGFs through cross-correlation. For this purpose we analyze EGFs obtained from windows of ambient noise, direct surface waves, or surface wave coda. Cross-correlation of (direct) surface wave windows yield EGFs (only) for direct surface wave propagation, but by changing the data window we can manipulate the parts of the wavefield that contribute to the construction of the EGF. Cross-correlation of coda waves should yield EGFs that include scattered waves. The latter can also be obtained by correlation of long records of ambient noise. In principle, coda wave and (pure) ambient noise correlation should produce similar EGFs and differences between them can give information about the energy distribution and heterogeneity under and near the array. We complement our analysis with plane wave beamforming (in the frequency–wavenumber domain), which quantifies the directional energy distribution of the signals that contribute to the EGF. This beamforming analysis reveals (temporal) variations in source regions of ambient noise, which – in turn – help understand the (changes in) symmetry and signal-to-noise ratio (SNR) of the EGFs.

2. Data and processing

We use 10 months (November 2003 to August 2004) of continuously recorded, vertical component broad-band data from a temporary seismograph array in southeastern (SE) Tibet (see Fig. 1). The 25 station array, with average station spacing ~100 km, was

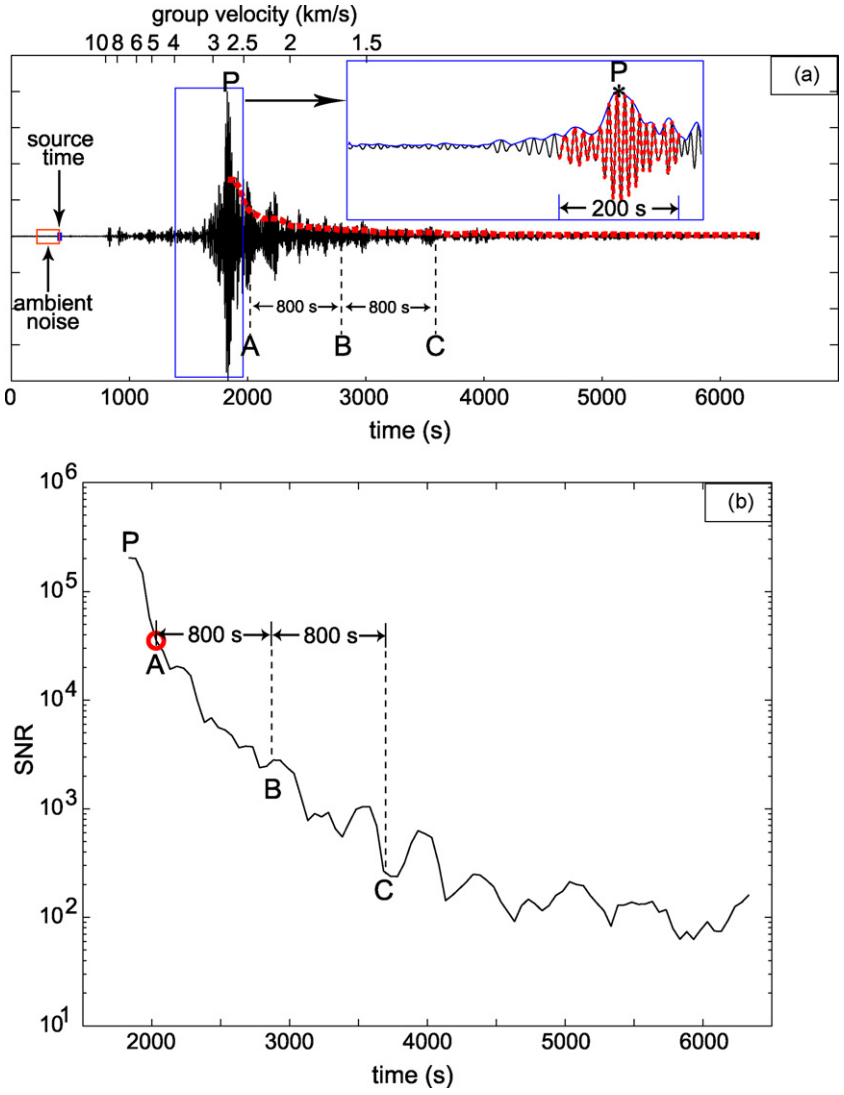

Fig. 2. Illustration of time windows used for the EGF retrieval. The seismogram in (a), band-pass filtered in the period band 10–20 s, is recorded by the station MC04 shown in Fig. 1 and the earthquake is located at (37.74°N, 143.08°E) with the magnitude m_b = 5.9. The epicentral distance is 3900 km. The bottom and top horizontal axes in (a) show the recording time and the corresponding group velocity (or horizontal propagation speed) of the records, respectively. The earthquake started at t = 400 s on the records. The seismogram in the inset figure of (a) shows the recordings in the 2.5–4 km/s group velocity window, which includes mainly direct surface waves, and the blue curve shows the envelope of the windowed recordings. The red dashed trace (200 s in length) in the inset figure, which centers at the point P corresponding to the maximum amplitude of the envelope, is selected as the direct surface waves for the retrieval of the Green's function. The red dashed curve in (a) is the root-mean-square (RMS) amplitude (using a 200 s running window) of the recordings after the maximum energy arrival point P. Here we define the surface wave coda starts at the point A, which is 200 s after P. The signal-to-noise ratio (SNR) of the coda is shown in (b), which shows apparent exponential decay of coda energy. The (ambient) noise window is defined as the 200 s window before the source time at 400 s, shown as the recordings in the red box in (a). For the retrieval of Green's function using surface wave coda, we select two time windows: the first and second 800 s window after A (the recordings within the window AB and BC, respectively). (For interpretation of the references to colour in this figure legend, the reader is referred to the web version of the article.)

deployed by MIT and the Chengdu Institute of Geology and Mineral Resources (CIGMR). For more detailed descriptions of the array data and the preliminary results from surface wave array tomography (ambient noise and traditional two-station analysis), which reveal strong heterogeneity in the crust, we refer to Yao et al. (2006, 2008).

Basic data pre-processing includes the removal of the mean and compensation for the instrument response. For the analyses presented here we first band-pass filter the data between periods of 10–20 s. Next, we select particular parts of the data (direct surface waves, surface wave coda, and ambient noise) from the continuous recordings, as shown in Fig. 2. Consider seismic waves released by an earthquake with source time, at t_s, recorded by a seismograph station at epicentral distance Δ (km). For any time t after t_s the corresponding average group velocity (or horizontal propagation speed) for 2D surface waves is $v_g = \Delta/(t - t_s)$, see Fig. 2. The example shows a main surface wave within window $v_g = (2.5\text{–}5.0)$ km/s. By muting (setting the amplitude of the seismic trace to zero) outside or inside a specific time window (e.g., Fig. 2), we select specific data windows associated with (known) earthquakes (e.g., Fig. 3) or (unknown) ambient noise. The detailed time window partitioning is given in Section 3.

We apply one-bit or normalized cross-correlation to the data band-pass filtered in these data windows to obtain the cross-correlation function. EGFs are then obtained from the time-derivative of the cross-correlation function by $-\hat{G}_{AB}(t) + \hat{G}_{BA}(-t) = (dC_{AB}(t)/dt)$, where $\hat{G}_{AB}(t)$ $(t \geq 0)$ is the causal part EGF at station B for a fictitious (point) source located at A, $\hat{G}_{BA}(-t)$ $(t \leq 0)$ is the anti-causal part EGF at A for a fictitious (point) source at B, and $C_{AB}(t)$ is the cross-correlation function between the two stations (Yao et al., 2006). Since for this analysis we use vertical component data we recover predominantly the Green's function for (fundamental mode) Rayleigh wave propagation. Similarly, Love waves can be recovered from transverse component data (Campillo and Paul, 2003; Paul et al., 2005; Lin et al., 2008).

3. EGFs from different data windows

In a heterogeneous medium, the Green's function for wave propagation between two points contains contributions from scattering anywhere in the medium—not just from structure located between the receiver points. EGFs are estimates of the Green functions obtained from correlation and summation of the diffuse wave-

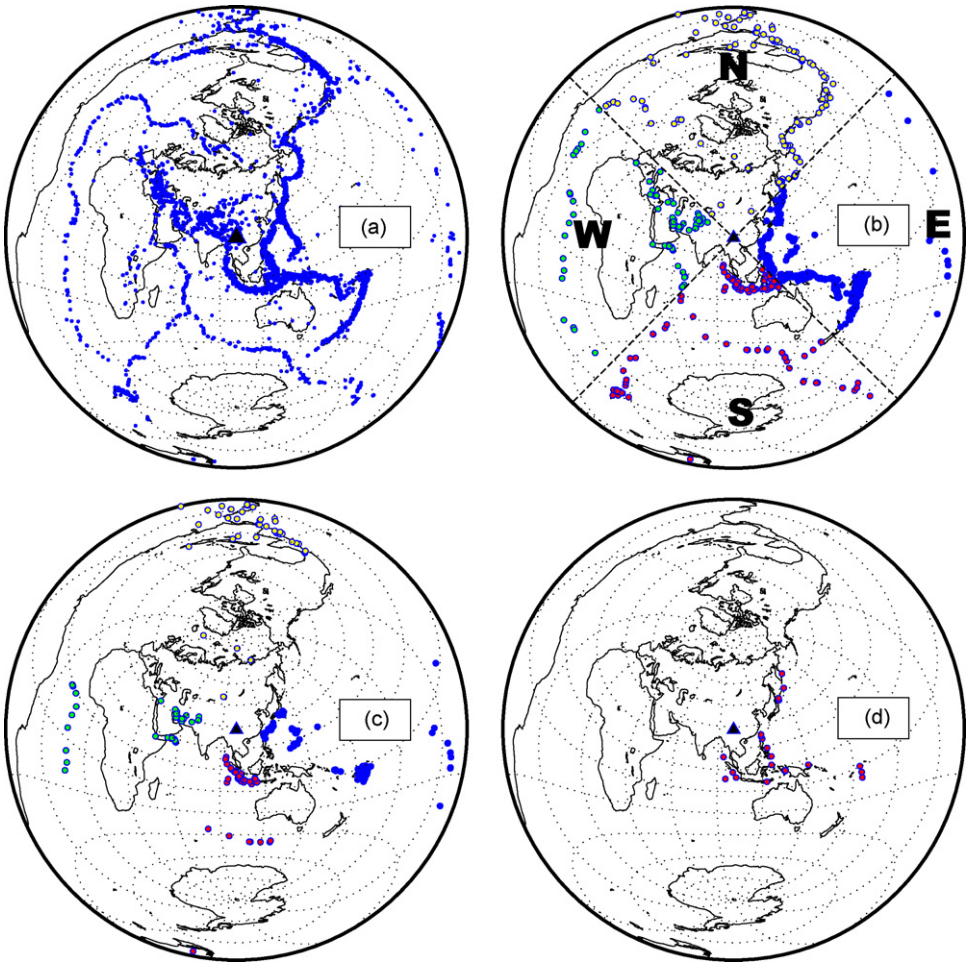

Fig. 3. (a) Epicenters of earthquakes with $m_b \geq 4$ (blue dots) that occurred in the 10 months from November 2003 to August 2004 (from EHB catalogue by Engdahl et al., 1998). The total number of earthquakes is about 7250. (b) Same as in (a) but for earthquakes with $m_b \geq 5$ and at least 2000 km away for the center of the array. The azimuth angle θ of the earthquake with respect to the center of the array satisfies $-45^\circ \leq \theta \leq 45^\circ$, $45^\circ \leq \theta \leq 135^\circ$, $135^\circ \leq \theta \leq 225^\circ$, and $225^\circ \leq \theta \leq 315^\circ$, for the earthquakes in the N, E, S, and W quadrants, shown as yellow, blue, red, and green dots, respectively. The total number of earthquakes in (b) is about 1000 and the number in the N, E, S, and W quadrants is 149, 577, 158, and 133, respectively. (c) Same as in (b) but only for the earthquakes near S–N or E–W direction (with respect to the array) with a maximum deviation angle of 22.5°. The number of earthquakes in the N, E, S, and W quadrants in (c) is 49, 120, 55, and 49, respectively. (d) Epicenters of 24 earthquakes ($m_b \geq 5$) for the retrieval of Green's function using surface wave coda (Section 3.4). The black triangle shows the location of the array. (For interpretation of the references to colour in this figure legend, the reader is referred to the web version of the article.)

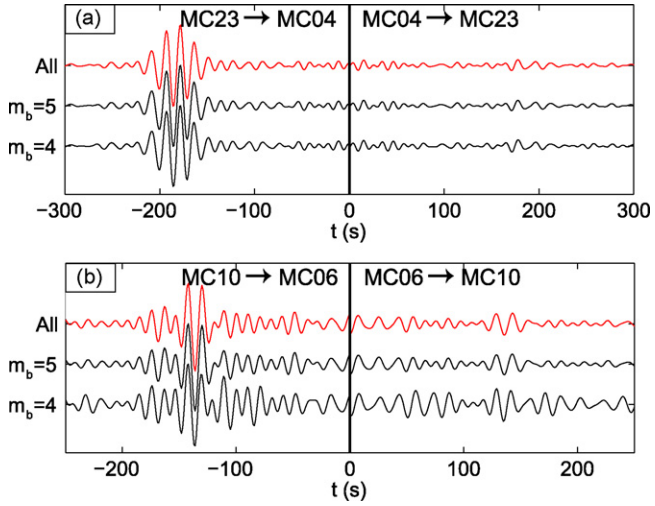

Fig. 4. EGFs (black traces) for the station pair (a) MC04–MC23 and (b) MC06–MC10 in the period band 10–20 s from approximately ambient noise after muting the wave trains in the 2–10 km/s group velocity window from earthquakes larger than the cut-off magnitude (m_b = 5 or 4, shown at the left side of each black trace) for all the 10 months data. The location of earthquakes is shown in Fig. 3a and b. The red traces in (a) and (b) are the EGFs from all the 10 months continuous data. The causal part shows for the EGF recorded at the station MC23 (or MC10) generated by a fictitious source at the station MC04 (or MC06) while the anti-causal part for recordings at MC04 (or MC06) with the source at MC23 (or MC10), same as shown in Figs. 5–7. (For interpretation of the references to colour in this figure legend, the reader is referred to the web version of the article.)

fields recorded at two receivers. How well the EGF is similar to the actual Green function strongly depends on the characteristics of the energy in the wavefields used. EGFs from cross-correlation of field data usually show a strong dependence on (non-uniform) energy distribution (Yao et al., 2006; Yao and Van der Hilst, 2009).

In this section we evaluate EGFs extracted from cross-correlation of data in different time windows. From the continuous records, we extract data associated with ambient noise, direct surface waves, and surface wave coda. We illustrate our analysis with data from two-station pairs (Fig. 1): MC04–MC23 (a N–S (north–south) pair with inter-station distance ~570 km) and MC06–MC10 (a W–E (west–east) pair with distance ~400 km).

3.1. EGFs from all continuous data

For reference, we first calculate EGFs for the two-station pairs from one-bit cross-correlation of the entire 10-month record, shown as the red trace in Fig. 4a and b for MC04–MC23 and MC06–MC10, respectively. Like other normalized cross-correlation methods (e.g., Bensen et al., 2007) one-bit cross-correlation normalizes the energy of all sources contributing to the construction of the EGF, so that the average energy flux is an indicator of the number (or the sum of normalized energy) of these sources, not their real magnitude. For both station pairs, the EGFs reveal Rayleigh wave arrivals with group speed around 3 km/s. Neither EGF is time-symmetrical, however, and the amplitude (or SNR) in the anti-causal part is much larger than in the causal part. For MC04–MC23 the 10-month average energy flux seems much higher from S to N (which contributes to the recovery of the anti-causal part of the EGF) than from N to S (the causal part). For MC06–MC10 the average energy flux in the 10 months is larger from E to W than from W to E.

3.2. EGFs from ambient noise

In the previous section we used continuous 10-month records. In this section and the next, we partition the data in specific energy propagation regimes (ambient noise, direct surface waves, and surface wave coda). The group velocity window procedure described above allows us to obtain EGFs (mostly) from ambient noise by suppressing signals associated with large earthquakes (see also Yao et al., 2006). Most direct body waves and surface waves, as well as their coda, appear in the group velocity window 2–10 km/s (see Fig. 2). Using earthquake origin times t_s from the EHB catalog by Engdahl et al. (1998) we mute signal within the 2–10 km/s group velocity windows for earthquakes larger than a certain magnitude. One-bit cross-correlation to the remaining signals is then used to extract EGFs (approximately) from ambient noise.

Note that ambient noise is here defined as all seismic energy unrelated to earthquakes with magnitude larger than the cut-off magnitude. Thus defined, ambient noise contains contributions from small earthquakes, but the smaller the cut-off magnitude the closer the remaining seismograms are to ambient seismic noise proper. The energy from such a source distribution approximately corresponds to the diffuse wavefield theoretically required for accurate Green's function construction. In this study we set the smallest cut-off magnitude to $m_b = 4$, because many earthquakes smaller than $m_b = 4$ are not listed in the EHB catalogue and recorded signals from those small earthquakes are usually below the ambient noise level due to the attenuation and geometrical spreading over a few thousand kilometers.

EGFs obtained from 10-month records of ambient noise, as defined above, are shown as the black traces in Fig. 4 for two cut-off magnitudes $m_b = 5$ and $m_b = 4$. The distribution of earthquakes with $m_b \geq 4$ and $m_b \geq 5$ is shown as in Fig. 3a and b, respectively. These EGFs are almost identical to the EGFs from the continuous 10-month records (red traces in Fig. 4). This implies that in the period band considered (10–20 s) the contributions from large earthquakes is small compared to that from ambient noise, as expected from one-bit cross-correlation (see also Yao et al., 2006). This also implies that the asymmetry of the EGFs is not caused by non-uniform distribution of large earthquakes but (for the time period considered) by ambient noise directionality, with most noise sources to the south and east of the array. Furthermore, tests (not shown here) with 1-month records showed that variations of EGFs over time are not related to the temporal variations in earthquake activity. In fact, (plane wave) beamforming with the EGFs (see Section 4 below) demonstrates that the temporal changes in EGF symmetry and amplitude are related to seasonal variations of ocean microseisms (see also Stehly et al., 2006; Pedersen et al., 2007). Together, these results suggest that for T = 10–20 s ambient noise is dominated by primary microseisms, which are usually attributed to coupling of oceanic wave energy into seismic energy in the Earth in shallow waters (Cessaro, 1994; Bromirski et al., 2005).

3.3. EGFs from direct surface waves

Earthquakes are distributed along plate boundaries (Fig. 3a) and because of this uneven geographical distribution Green's function reconstruction from direct surface waves is often incomplete. To study the EGFs from surface waves the data selection is almost the opposite of what we did in the previous section; we keep only the data inside the 2.5–5 km/s group velocity window (calculated for earthquakes with $m_b \geq 5$, Fig. 3b). This window contains mainly the (dispersive) surface wave fundamental mode (Fig. 2a). From stationary phase analysis it is easily understood that the strongest contribution for a particular station pair comes mainly from sources located on or near the line connecting the stations (Snieder, 2004). For a given seismic station pair we can, therefore, choose the direction from which we want contributions. For this purpose we divide the earthquake source regions into E, S, W and N quadrants (Fig. 3b). As before, one-bit normalization is used to the records before cross-correlations.

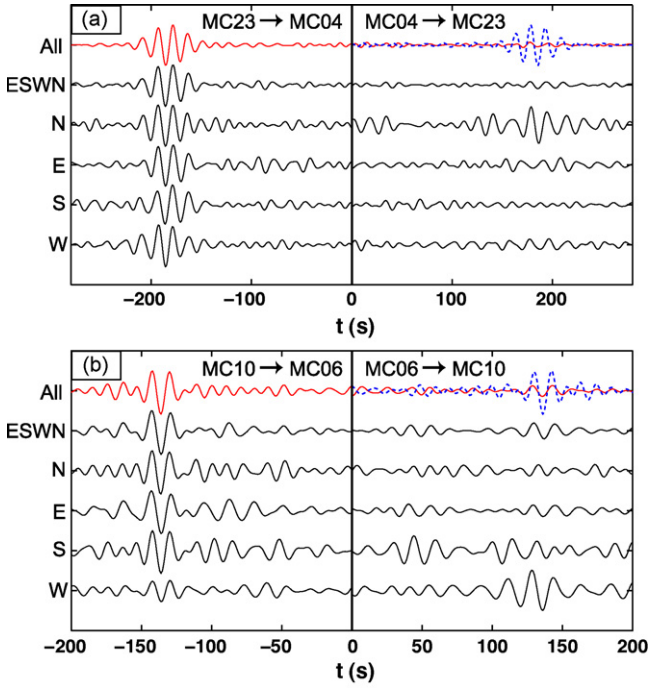

Fig. 5. EGFs (black traces) in the period band 10–20 s for the station pair (a) MC04–MC23 and (b) MC06–MC10 only from direct (minor-arc) surface waves in the 2.5–5 km/s group velocity window from the earthquakes with $m_b \geq 5$ in the 10 months in the world (labeled as 'ESWN' at the left side), and from four different quadrants (labeled as 'N', 'E', 'S', and 'W' at the left side; for location of earthquakes in each quadrant, see Fig. 3b). The red traces in (a) and (b) is the same as that shown in Fig. 4a and b, respectively. The blue dashed traces in (a) and (b) is the time reversal of the anti-causal EGF of the red trace, shown as the reference for the causal part EGF. (For interpretation of the references to colour in this figure legend, the reader is referred to the web version of the article.)

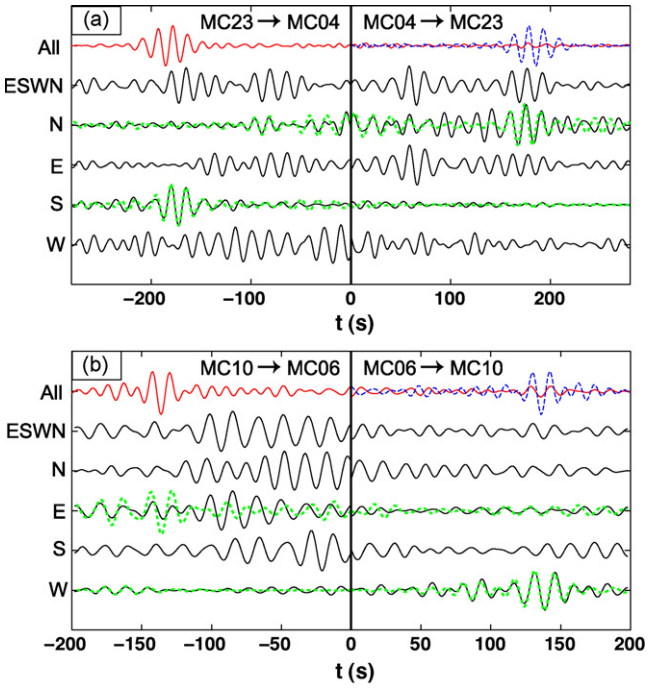

Fig. 6. Similar as shown in Fig. 5, but for EGFs (black traces) recovered from direct surface waves in a more rigorously defined window from large earthquakes (see Fig. 2a and Section 3.3). The green dashed trace labeled as 'N' (or 'S') in (a) is the EGF for MC04–MC23 from earthquakes in the N (or S) quadrant only near the S–N direction within 22.5° deviation (red or yellow dots in Fig. 3c). The green dashed trace labeled as 'E' (or 'W') in (b) is the EGF for MC06–MC10 only using earthquakes in the E (or W) quadrant near the E–W direction (blue or green dots in Fig. 3c). The top red and blue traces are the same as shown in Fig. 5. (For interpretation of the references to colour in this figure legend, the reader is referred to the web version of the article.)

For both station pairs, the EGFs from all earthquake data (Fig. 5, black traces labeled as 'ESWN') show a similar time-asymmetry as EGFs from the 10-month continuous data (Fig. 4, red traces). For MC04–MC23 the anti-causal part of the EGF from earthquake data in each quadrant is similar to the anti-causal part from all data (Fig. 4a). However, the causal part (that is, surface waves propagating from N to S) can only be recovered from the earthquakes in the N quadrant (yellow circles in Fig. 3b). Seismicity in the north is relatively low and the earthquakes used are mostly far away from the array. We still observe a causal phase around the same time as the reference phase (Fig. 5a, blue trace), but it is much noisier than the anti-causal part. For the E–W station pair we can make similar observations (Fig. 5b). The anti-causal EGF from earthquakes in the E, S, and N quadrants are, again, similar to that from all data. Data from events in the W quadrant produce both a causal and anti-causal part (Fig. 5b, black trace labeled as 'W'), but the latter is substantially weaker. This demonstrates that we can indeed recover the (anti-) causal parts of the surface wave Green's function by using earthquake data from a specific direction.

The fact that for both the N–S and E–W station pairs we can recover anti-causal surface wave EGFs for all seismicity quadrants is surprising. In principle, energy from directions perpendicular to the geographical orientation of the receiver pair contributes little to the Green's function of (surface) wave propagation between them. We speculate that the successful recovery of anti-causal EGFs is due to presence of ambient noise energy in the 2.5–5 km/s group velocity window.

To suppress this contamination by ambient noise energy we define a more rigorous direct surface wave window (Fig. 2a), which centers at the maximum energy arrival within the group velocity window 2.5–4 km/s in the period band 10–20 s calculated for each earthquake with $m_b \geq 5$ (Fig. 3b). This new window is only 200 s long and contains only the most energetic part of the direct surface waves from large earthquakes. Instead of applying one-bit normalization to the records, which tends to enhance ambient noise energy, we normalize the records in this direct surface wave window by dividing by the maximum amplitude in that window before cross-correlations. Fig. 6 shows the EGFs from the correlation of recordings in this new direct surface wave window.

For the S–N station pair MC04–MC23, the EGF constructed from the direct surface waves from all earthquakes in Fig. 3b shows quite a symmetric surface wave arrival around 178 s (the trace labeled as 'ESWN' in Fig. 6a), although spurious earlier arrivals appear in both the causal and anti-causal parts. These early arrivals are probably due to surface wave energy coming from earthquakes in subduction zones along Japan, Kuril trench, Aleutian trench, and the eastern Pacific coastline (contributing to the early arrival in the causal part EGF), and earthquakes around the Philippine, New Guinea, Solomon Islands, and Tonga trenches (contributing to the early arrival in the anti-causal part EGF). Unlike the results shown in Fig. 5a, in which the anti-causal part EGF seems to be recovered due to the presence of ambient noise energy, the anti-causal part EGF in Fig. 6a (the black trace labeled as 'S') is recovered from direct surface waves propagating from S to N from the earthquakes in the S quadrant (Fig. 3b). Similarly, the causal part EGF in Fig. 6a (the black trace labeled as 'N') is recovered by the earthquake data in the N quadrant (Fig. 3b) but has much lower SNR than that of anti-causal EGF recovered from the earthquake data in the S quadrant. This is probably due to the larger epicentral distances for the earthquakes in the N quadrant. Earthquakes along the Kuril and Aleutian trenches

and the eastern Pacific coastline, with back azimuths ∼45° off the inter-station direction, tend to produce (spurious) early arrivals in the causal part EGF.

For the E–W station pair MC06–MC10 the recovery of EGFs using the new surface wave window (Fig. 6b) is also quite different from that using the 2.5–5 km/s group velocity window (Fig. 5b). This reflects the uneven distribution of earthquakes (Fig. 3b), not ambient noise energy. Dominant early arrivals appear in the anti-causal EGFs inferred both from all earthquakes in Fig. 3b and for earthquakes restricted to the N, E, or S quadrants. This reflects the fact that a large number of earthquakes exist with large angles (about 45°) off the E–W inter-station direction in the subduction zones along the western Pacific Ocean (Fig. 3b). The causal EGF (the black trace labeled as 'W' in Fig. 6b) from earthquakes in the W quadrant is very well recovered and the anti-causal part EGF almost disappears, which implies that the contamination of ambient noise energy in this new surface wave window is very small.

Stationary phase analysis implies that only sources locating near or along the (surface wave) ray path connecting the stations contribute to the reconstruction of the Green's function of that station pair (Snieder, 2004; Yao and Van der Hilst, 2009). Sources within the first Fresnel zone of interferometry constructively contribute to the recovery of the Green's function and the width of the first Fresnel zone depends on the inter-station distance and the frequency of waves considered (Yao and Van der Hilst, 2009). Sources far away from the inter-station ray path either interfere destructively (for even source distribution) or produce spurious early arrivals (for uneven source distribution), as shown in Fig. 6b. Therefore, through careful selection of earthquakes along the inter-station ray path, we can recover the Green's function and suppress (spurious) early arrivals. For example, for the S–N station pair MC04–MC23 we only select earthquakes near the S–N direction (less than 22.5° deviation); similarly, for the E–W station pair MC06–MC10 only earthquakes near the E–W direction (less than 22.5° deviation) are used (Fig. 3c). For the S–N station pair MC04–MC23 the re-selected earthquakes in the N (or S) quadrant recover the causal (or anti-causal) part EGF (the green dashed trace labeled as 'N' (or 'S') in Fig. 6a). Similarly, for the E–W station pair MC06–MC10 the re-selected earthquakes in the E or W quadrant recover the anti-causal or causal part EGF (the green dashed trace labeled as 'E' or 'W' in Fig. 6b). In particular, the anti-causal part EGF is very well recovered and the early arrivals almost disappear. For the estimation of Green's function between two stations, this "steered" seismic interferometry with direct waves from selected earthquakes provides an alternative to ambient noise interferometry.

3.4. EGFs from coda waves

Independent of the source distribution, one can improve the conditions for Green's function construction by exploiting wavefield scattering due to medium heterogeneity (Campillo and Paul, 2003; Paul et al., 2005). Coda waves are due to (multiple) scattering in the shallow subsurface (Sato and Fehler, 1998) and can be divided into two regimes (Malcolm et al., 2004): an earlier diffusion regime and a later equipartitioning regime. The equipartitioning regime is theoretically the optimal regime for interferometric Green's function reconstruction because no preferred direction and mode of propagation exists (Van Tiggelen, 2003).

For surface wave applications in solid Earth seismology the diffusion regime is usually found in the (late) coda of direct S (Campillo and Paul, 2003; Paul et al., 2005) or Rayleigh waves (Langston, 1989). Equipartitioning has indeed been observed in late coda waves from short-period S waves (Hennino et al., 2001), but the associated energy usually falls below the ambient noise level because it arrives many mean-free times after the direct waves. As a consequence, EGFs from late coda often show the same directional bias as EGFs from ambient noise (e.g., Paul et al., 2005).

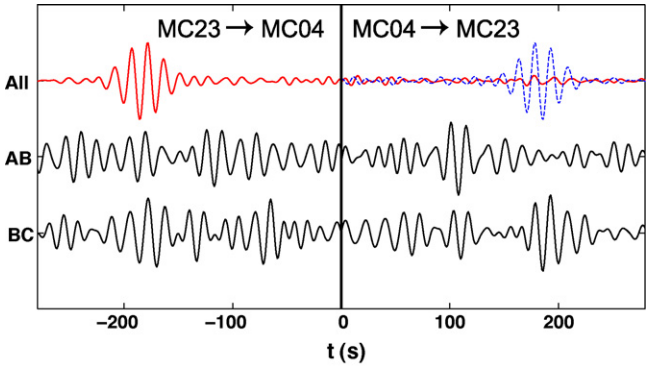

Fig. 7. EGFs (black traces) in the period band 10–20 s for MC04–MC23 from surface wave coda of the large earthquakes ($m_b \geq 5$, red dots in Fig. 3d) in two different time windows (AB and BC, each with 800 s length) shown at the left side of each black trace. The detailed definition of these two coda windows is given in Fig. 2 and Section 3.4. The coda in the window AB and BC is the earlier and later part of surface wave coda, respectively.

Using the S–N station pair MC04–MC23 as an example, we investigate the correlation of coda from the selected earthquakes (Fig. 3d) in two 800 s long coda windows (AB and BC in Fig. 2). For each selected earthquake we require that (1) the root-mean-square (RMS) amplitude of surface wave coda in the first 2000 s window shows an indication of exponential decay (Fig. 2b), (2) the SNR of the direct surface wave arrival has to be larger than 1000, and (3) the minimum SNR within each 800 s coda window is larger than 50. The reason for these strong requirements is to suppress the effect of ambient noise energy in coda waves on the reconstruction. Thus the surface wave coda from 24 large earthquakes (Fig. 3d) is used for the retrieval of Green's functions. Before cross-correlating coda waves we normalize their amplitudes by dividing by the RMS amplitude (the red dashed line in Fig. 2a).

The recovered EGFs from the earlier coda window (AB) and the later coda window (BC) are shown in Fig. 7, which seem to have much lower SNR compared to EGFs inferred from all 10 months of data. In contrast to the (reference) arrival from ambient noise (blue trace in Fig. 7) the causal EGF from the earlier coda (the trace labeled as 'AB') does not show an apparent surface wave arrival around 178. The anti-causal EGF from the earlier coda results in surface wave arrivals similar to that of the reference arrival (red trace in Fig. 7), but appears to be too noisy. However, the recovery from the later coda is much improved. Both the causal and anti-causal part EGF from the later coda (the trace labeled as 'BC') show surface wave arrivals that are similar (also in amplitude) to the reference arrival from ambient noise. This indicates that the later coda (in the second 800 s coda window) is sufficiently diffuse to construct both the causal and anti-causal part EGFs, while the scattered energy in the earlier coda (in the first 800 s coda window) may be still dominated in some specific directions related to the direction of incoming energy and local heterogeneities. For both coda windows the SNR of coda to ambient noise is sufficiently large (at least 50), and the contribution from ambient noise energy appears to be negligible.

4. Seasonal variability and origin of ambient noise energy

The energy density and distribution of ambient noise – and as a consequence, the reliability of EGFs from wavefield cross-correlation – varies with frequency and time. In this section we investigate the temporal changes in the directional distribution and origin of ambient noise energy (in the period band 10–20 s)

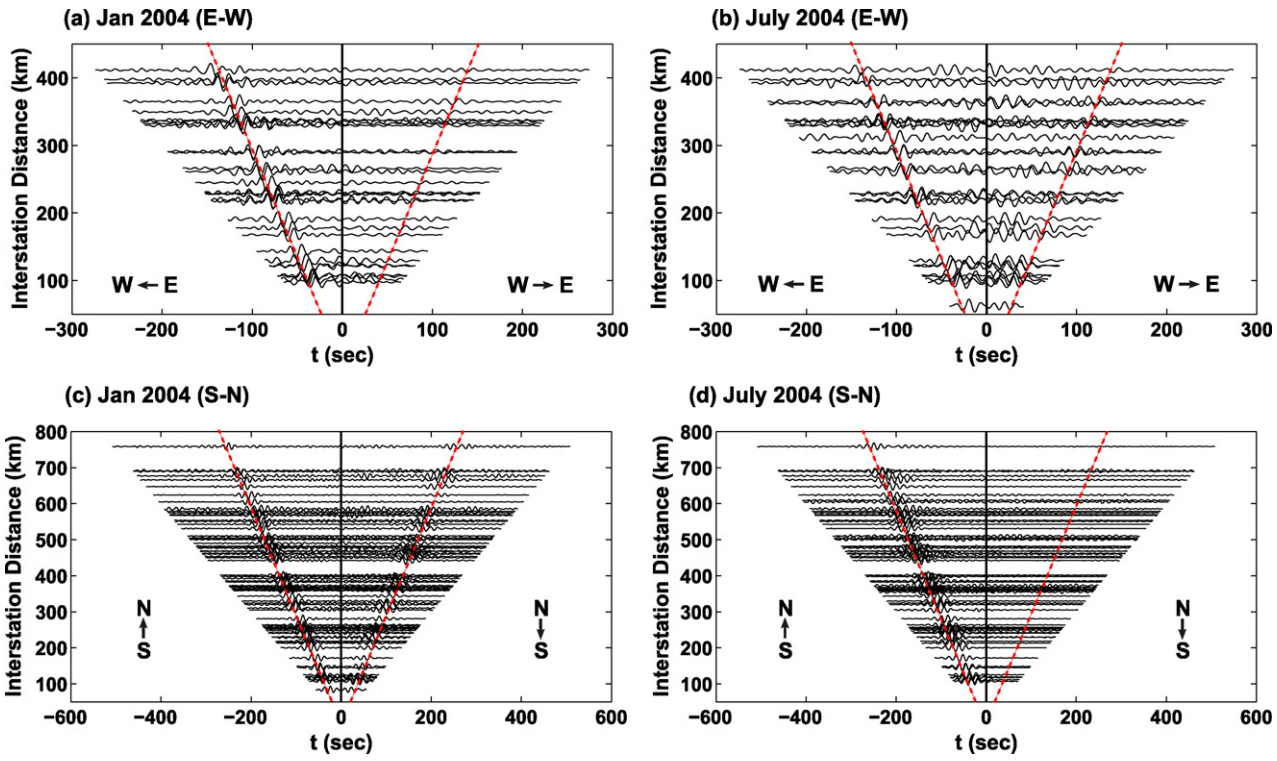

Fig. 8. Comparison of cross-correlation functions in the period band 10–20 s from 1 month data of (a) January 2004 for E–W two-station pairs, (b) July 2004 for E–W two-station pairs, (c) January 2004 for S–N two-station pairs, and (d) July 2004 for S–N two-station pairs. Here the E–W or S–N two-station pairs are station pairs directed roughly from E to W or N to S with a maximum of 15° deviation. 'E → W' means the fictitious noise sources approximately to the E of the array generate waves propagating to the W for the retrieval of the anti-causal EGF as shown in (a) or (b), similarly for 'W → E' but for the retrieval of the causal EGF in (a) and (b), 'S → N' for the anti-causal EGF in (c) and (d), and 'N → S' for the causal EGF in (c) and (d).

with respect to the MIT-CIGMR array in SE Tibet. We first analyze the variations of the amplitude of one-bit cross-correlation functions (CFs) over time (Figs. 8 and 9). Subsequently we perform a (frequency–wavenumber) beamforming analysis in order to constrain the temporal variations in the geographical origin of the ambient noise energy (Fig. 10).

As in Stehly et al. (2006), we analyze the symmetry and amplitude of CFs using data band-passed between 10 and 20 s (the frequency band of the primary microseisms) during different seasons. We correlate 1 month of continuous records during the northern hemisphere summer (July 2004) and northern hemisphere winter (January 2004) for station pairs directed roughly from north to south and east to west (with 15° deviation). In the winter, the CFs for the E–W station pairs are dominated by energy traveling from the east, as is evident from the one-sided CFs (Fig. 8a). For the E–W station pairs, the summer CFs (Fig. 8b) have lower SNR than in the winter but do not seem to have a preferred direction, and (weak) very early arrivals become apparent. The CFs calculated for the N–S station pairs show fairly good symmetry in winter (see Fig. 8c) indicating a similar energy flux into the array from the south or north. In summer time, the apparent asymmetry of the CFs (Fig. 8d) indicates that energy coming from the south is much larger than from the north.

The traces in Fig. 8 correspond to E–W and N–S station pair orientations, but pie charts illustrate the azimuthal dependence of the normalized amplitude of the CFs (or ambient noise energy flux) for all station pairs, both for winter (Fig. 9a) and summer (Fig. 9b). The background image in Fig. 9 shows the distribution of the normalized global ocean wave height, modified after Stehly et al. (2006). The pie charts show that the ambient noise energy in the winter (Fig. 9a) is more uniformly distributed than in the summer (Fig. 9b). In the winter, noise energy is dominant in the east and north-east directions (possibly related to enhanced wave power in the Northern Pacific) and also from the south (Indian Ocean) and the north (Northern Atlantic). In the summer, the main direction of the ambient noise energy is from the south–southwest, pointing to an origin in the Indian Ocean. These results are consistent with the observations of Stehly et al. (2006) and Yang and Ritzwoller (2008).

To confirm, quantify, and interpret the above illustration of seasonal CF amplitude variations, we perform a wavenumber–frequency analysis of the same data. Wavenumber–frequency analysis of random noise fields decomposes the wavefield into plane waves, which allows one to characterize the noise wavefield – or the wavenumber–frequency power-spectral density – by an azimuth and apparent slowness (or velocity) (Lacoss et al., 1969; Aki and Richards, 1980; Johnson and Dudgeon, 1993). We divide approximately 1 month of data (January 2004 or July 2004) into 512 s windows with an overlap of 100 s. Using the algorithm due to Lacoss et al. (1969) we beamform the data in these windows for 20 central periods between 10 and 20 s using a narrow band-pass filter of about 0.002 s. The angle resolution is 2°, while the velocity resolution is 20 m/s. The beamforming results in all time windows and frequency bands are then normalized and stacked to produce the final images of the power of the noise wavefield in the period band 10–20 s in terms of velocity in m/s along the radial axis and azimuth in degrees, along the angle, shown in Fig. 10.

Fig. 10a and b shows the noise power during January 2004 and July 2004, respectively. The wavefield is dominated by energy coming from the south–southwest during the July 2004 (Fig. 10b), in excellent agreement with results of the above analysis of CF amplitudes (Fig. 9b). The apparent velocity is around 3200 m/s, which agrees very well with the velocities obtained from dispersion analysis (see Figs. 11b and 12b). The noise power during January 2004 has less obvious directionality (Fig. 10a). The same direction in the south–south east causes arrivals with velocities around 3200 m/s,

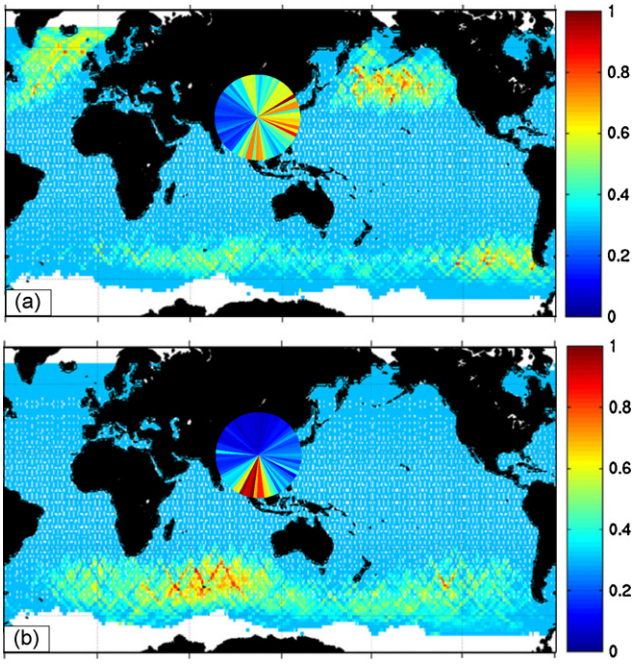

Fig. 9. Seasonal variation of the azimuthal dependence of the normalized amplitude of the cross-correlation functions (shown as the pie chart) for all possible MIT-CIGMR array station pairs: (a) in northern hemisphere winter time (January 2004) and (b) in northern hemisphere summer time (July 2007). The pie charts are constructed using the procedure from Stehly et al. (2006) by averaging the amplitude of all CFs in each azimuthal sector (5° width here) with a geometrical spreading amplitude correction considering the difference in inter-station distance. The background image shows the distribution of the normalized global ocean wave height in winter time (a) and in summer time (b) (modified after Stehly et al., 2006). The colour bar in the right gives the value of normalized amplitude for both cross-correlation functions and the ocean wave heights. In the pie chart, the red sector at certain azimuth angle approximately implies that more energy is coming from that azimuth angle and propagating into the array (center of the pie chart). (For interpretation of the references to colour in this figure legend, the reader is referred to the web version of the article.)

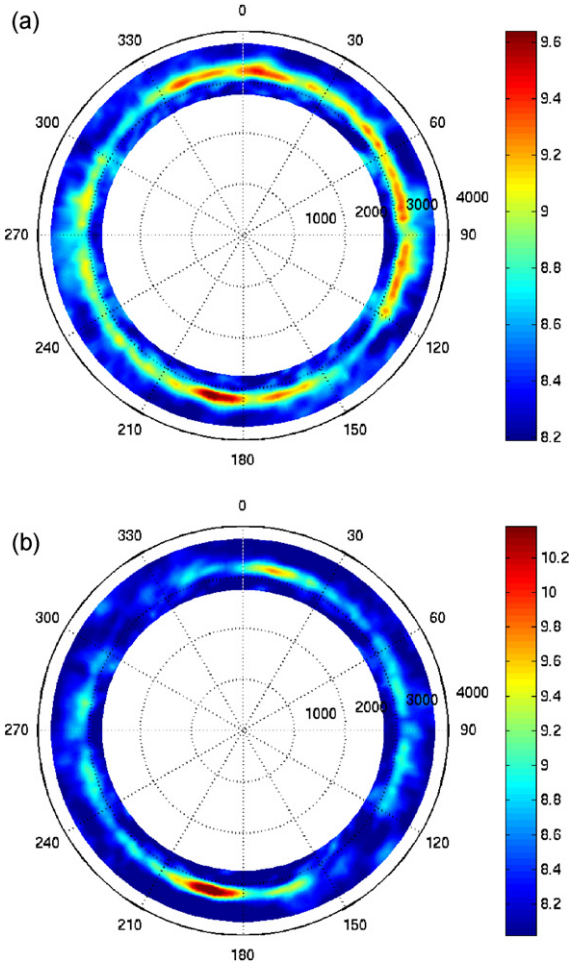

Fig. 10. (a) Noise power from beamforming analysis in January 2004, for the period band 10–20 s. The noise mainly arrives from the south–southwest and from between the north–northwest and east–southeast. The apparent velocity is around 3200 m/s. (b) Noise power from beamforming analysis in July 2004, for the period band 10–20 s. The noise mainly arrives from the south–southwest. The apparent velocity is around 3200 m/s.

but significant energy also arrives from the north and east with approximately equal amounts and much weaker energy flux from the west. This is also similar to the result from the above CF analysis (Fig. 9a). Overall, the noise power in January is less than during July.

The above observations that the CFs for E–W station pairs have a lower SNR in the summer (Fig. 8b) than in the winter (Fig. 8a) and that early arrivals appear in the summer time CFs may both be explained by the overall dominance of energy from the south in the summer, as established by the beamforming. If plane waves arrive from the south–southwest at an E–W station pair, the result will be an arrival with very high apparent velocity (and thus early arrival time).

5. Discussion

We evaluated the recovery of (surface wave) Green's functions from ambient noise, direct surface waves, and surface wave coda (for T = 10–20 s). Fig. 11a shows the EGFs recovered from different data windows for the S–N station pair MC04–MC23. The EGFs from the different data windows give similar surface wave arrival times (around 178 s). However, the arrival time of the EGF (labeled as 'S−' in Fig. 11a) recovered from direct surface waves using the earthquakes in the S quadrant (see Fig. 3c) appears several seconds later than the reference travel time of the EGF from ambient noise. The arrival time of the EGF (labeled as 'N+' in Fig. 11a) using earthquakes in the N quadrant appears a few seconds earlier. Dispersion analysis for the various EGFs in Fig. 11a shows differences among the phase velocities (Fig. 11b) with a standard deviation about 1–2% of the average phase velocities. Indeed, the phase velocities of the 'N+' EGF (Fig. 11a) are about 1–1.5% higher than the average and for the 'S−' EGF (Fig. 11a) the phase velocities are 0.5–1.5% lower. This difference reflects the difference of source distribution (Fig. 3c) for the construction of surface wave Green's function through cross-correlation. The phase velocities of the causal and anti-causal EGFs from coda waves also show up to 1.5% difference, implying the difference of (scattered) energy for the Green's function retrieval. If the scattered wavefield in the late coda is isotropic and well above the ambient noise level, we would expect the same dispersion characteristics for the causal and anti-causal part EGFs. However, in reality, attenuation and existence of ambient noise energy usually result in some predominant directions of energy propagation in the late coda.

In theory the causal and anti-causal parts of the Green's function are the same. However, in practice, the recovered EGFs from cross-correlation of different data windows may be different (Figs. 4–7) indicating non-isotropic energy propagation. To improve the quality of dispersion analysis of the EGFs from seismic interferometry, one usually stacks the causal and anti-causal part EGFs to enhance the SNR and suppress the effect of uneven source distribution or energy propagation (e.g., Yang et al., 2007; Yao et al., 2008). Here we stack the causal and anti-causal part EGFs from ambient noise, direct surface waves, or surface wave coda, as shown in Fig. 12a.

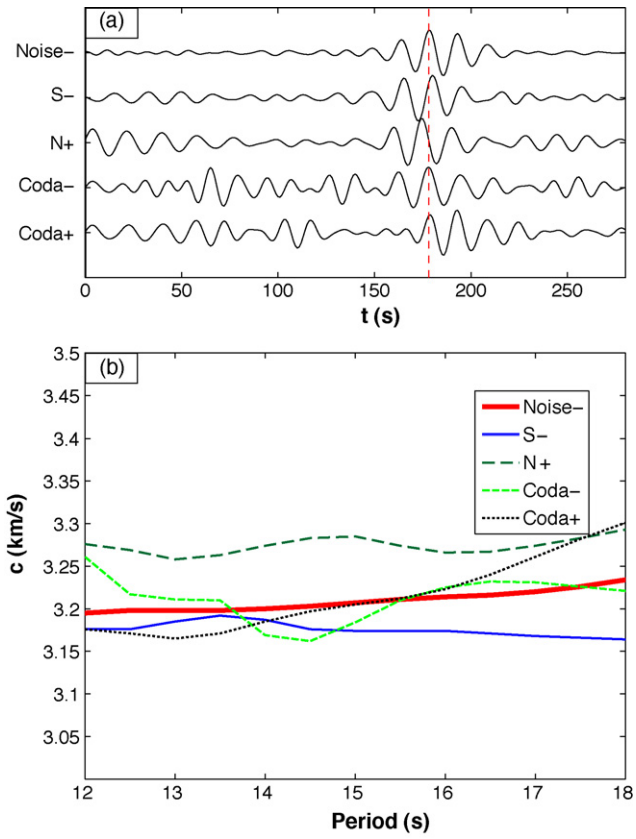

Fig. 11. (a) Comparison of the EGFs of MC04–MC23 constructed from cross-correlations of different data windows: 'Noise−' for the anti-causal part EGF labeled as 'm_b = 4' in Fig. 4a, 'S−' for the anti-causal part EGF (green dashed trace) labeled as 'S' in Fig. 6a, 'N−' for the causal part EGF (green dashed trace) labeled as 'N' in Fig. 6a, 'Coda−' for the anti-causal part EGF labeled as 'BC' in Fig. 7, and 'Coda−' for the causal part EGF labeled as 'BC' in Fig. 7. (b) Phase velocity dispersion curves in the period band 12–18 s for the EGFs in (a). The red dashed line in (a) shows the reference travel time (at 178 s) corresponding to the point with the maximum amplitude of the EGF labeled as 'Noise−'. (For interpretation of the references to colour in this figure legend, the reader is referred to the web version of the article.)

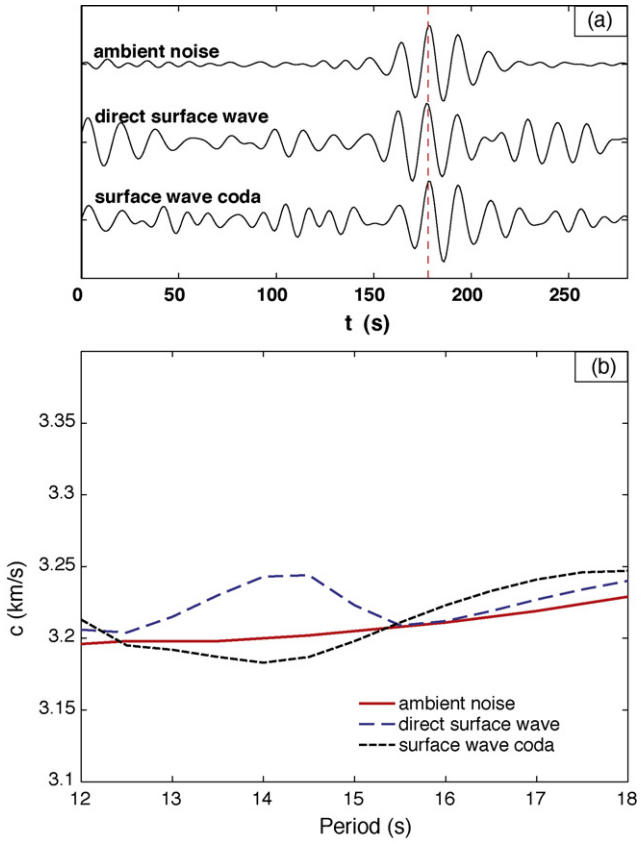

Fig. 12. (a) Comparison of the stacked EGFs of MC04–MC23 constructed from three different data windows, i.e., ambient noise (top trace, stack of the causal and anti-causal parts of the bottom trace in Fig. 4a labeled as 'm_b = 4'), direct surface wave (middle trace, stack of the two traces labeled as 'S−' and 'N+' in Fig. 11a), and surface wave coda (bottom trace, stack of the two traces labeled as 'Coda−' and 'Coda+' in Fig. 11a). (b) Comparison of phase velocity dispersion in the period band 12–18 s of the stacked EGFs in (a). The red dashed line in (a) shows the reference travel time (at 178 s) corresponding to the point with the maximum amplitude of the stacked EGF labeled as 'ambient noise'. (For interpretation of the references to colour in this figure legend, the reader is referred to the web version of the article.)

The stacked EGFs from different data windows have very similar arrival times (the difference is less than 1 s, Fig. 12a) and the SNR is also improved, especially for the stacked EGF using coda waves. The phase velocity dispersion curves between the stacked EGFs from ambient noise and surface wave coda are very similar with less than 1% difference (Fig. 12b). The phase velocities around 14 s of the stacked EGF from direct surface waves are about 1.5% higher than from ambient noise or surface wave coda, but at other periods their differences are quite small (less than 0.5%). This suggests that stacking the causal and anti-causal parts of the EGFs does, indeed, improve the quality of dispersion analysis.

By using different data windows we effectively manipulate the character of seismic energy that contributes to the construction of the EGF. This, in turn, also alters the type of information that can be retrieved about the medium. As we demonstrated in Figs. 11 and 12, EGFs can be retrieved successfully from continuous ambient noise, direct surface waves, or surface wave coda. The surface waves recovered from 10 months of ambient noise have higher SNR than those recovered from ground motion due to large earthquakes (with much shorter time length for cross-correlation). The SNR of the recovered surface waves from direct surface waves is also high (Fig. 11a). However, it is sometimes necessary to select the earthquakes (with back azimuths near the orientation of the two-station pair) to avoid the generation of spurious early arrivals (due to incomplete reconstruction) or bias from earthquakes with energy propagating perpendicular or at large angle from the station pair (Fig. 6). In practice, one can steer the known sources (e.g., larger earthquakes) within the regime of constructive interference to improve the recovery of the Green's function. The steering process may include both the selection of sources and compensation of source energy to enable the perfect recovery.

The SNR of the recovered surface waves from the later surface wave coda seems to be poor. However, the phase information can be well recovered (Figs. 11 and 12) and the causal and anti-causal parts are nearly symmetric. The early coda is expected to be dominated by single scattering, whereas in the late coda, multiple scattering contributes to the diffusion of energy. In theory a diffuse wavefield produces a more symmetric EGF (Sánchez-Sesma et al., 2008; Malcolm et al., 2004) and this is clearly observed here (Fig. 7). However, since multiply scattered energy decays faster and can quickly fall below the noise level, especially for the range of inter-station distances considered in our study, this really limits our selection of coda waves for the Green's function retrieval. The poor SNR of the EGF from coda waves is probably due to the very limited data we can use for the recovery (Fig. 3d) in order to minimize the contamination of ocean microseisms in the period band 10–20 s. The extent to which EGFs recovered from coda waves can be used in, for example, tomography is thus limited.

Our study illustrates that the comparison of EGFs extracted from different regimes in the seismic trace is complicated by var-

ious factors. Much depends on the frequency band one uses for the correlations. For periods between 10 and 20 s ambient noise is dominated by the primary microseism and effects of scattering are relatively weak. For shorter periods, scattering is stronger (due to the shorter wavelength compared to heterogeneity) and ocean generated ambient noise may be weaker if the array is far from the coastline. For shorter periods we may, therefore, expect to retrieve more symmetric EGFs with higher SNR from late coda data for station pairs with shorter distance considering high attenuation at shorter periods. At longer periods, say, from 20 to 120 s, the effect of scattering is less (Langston, 1989) and ambient noise energy generally shows weak (Yang and Ritzwoller, 2008) or no directionality (Pedersen et al., 2007). Therefore, in this period band one can use direct waves and noise to retrieve Green's functions.

6. Conclusions

We demonstrated that the surface wave empirical Green's function can be retrieved from cross-correlation of different data windows (ambient noise, direct surface waves, or surface wave coda) using array data from SE Tibet. Phase velocity dispersion also reveals similar dispersion characteristics of these empirical Green's functions. The directionality of ambient noise energy distribution may have a large effect on the recovery of the Green's function when one tries to use direct surface waves or coda waves due to large earthquakes. Therefore, proper windowing of earthquake data in different regimes is necessary for the Green's function recovery. By examining the symmetry and amplitude of the cross-correlation functions and performing a frequency–wavenumber beamforming analysis, we conclude that the dominant ambient noise field in the period band 10–20 s is from the ocean activities and shows clear seasonal dependence. The average phase velocity between 10 and 20 s of the study area from beamforming analysis is very similar to what we obtained from dispersion analysis. Wavenumber–frequency beamforming analysis of the noise wavefield helps in interpreting the empirical Green's function obtained from cross-correlation and provides important knowledge of the directionality of ambient noise energy.

Acknowledgments

We thank the editor Keke Zhang and three anonymous reviewers for their constructive comments, which helped us improve the manuscript. We also thank Dr. Pierre Gouedard at MIT for helpful discussion on coda wave analysis.

References

Aki, K., Richards, P.G., 1980. Quantitative Seismology, Theory and methods, vol. 1. W.H. Freeman, San Francisco, CA.
Bakulin, A., Calvert, R., 2006. The virtual source method: theory and case study. Geophysics 71 (4), SI139–SI150.
Bardos, C., Garnier, J., Papanicolaou, G., 2008. Identification of Green's functions singularities by cross correlation of noisy signals. Inverse Problems 24, 015011.
Bensen, G.D., Ritzwoller, M.H., Barmin, M.P., Levshin, A.L., Lin, F., Moschetti, M.P., Shapiro, N.M., Yang, Y., 2007. Processing seismic ambient noise data to obtain reliable broad-band surface wave dispersion measurements. Geophys. J. Int. 169, 1239–1260.
Bromirski, P.D., Duennebier, F.K., Stephen, R.A., 2005. Mid-ocean microseisms. Geochem. Geophys. Geosyst. 6, Q04009, doi:10.1029/2004GC000768.
Colin de Verdière, Y., 2006a. Mathematical models for passive imaging I: general background. URL http://fr.arxiv.org/abs/math-ph/0610043/.
Colin de Verdière, Y., 2006b. Mathematical models for passive imaging. II. Effective Hamiltonians associated to surface waves. URL http://fr.arxiv.org/abs/math-ph/0610044/.
Campillo, M., Paul, A., 2003. Long-range correlations in the diffuse seismic coda. Science 299, 547–549.
Cessaro, R.K., 1994. Sources of primary and secondary microseisms. Bull. Seism. Soc. Am. 84, 142–148.
De Hoop, M.V., De Hoop, A.T., 2000. Wave-field reciprocity and optimization in remoting sensing. Proc. R. Soc. Lond. A (Math. Phys. Eng. Sci.) 456, 641–682.
De Hoop, M.V., Solna, K., 2008. Estimating a Green's function from field-field correlations in a random medium. SIAM J. Appl. Math. 69 (4), 909–932.
Engdahl, E.R., Van der Hilst, R.D., Buland, R.P., 1998. Global teleseismic earthquake relocation from improved travel times and procedures for depth determination. Bull. Seism. Soc. Am. 88, 722–743.
Hennino, R., Trégourès, N., Shapiro, N., Margerin, L., Campillo, M., Van Tiggelen, B., Weaver, R.L., 2001. Observation of equipartition of seismic waves in Mexico. Phys. Rev. Lett. 86, 3447–3450.
Langston, C.A., 1989. Scattering of long-period Rayleigh waves in Western North America and the interpretation of coda Q measurements. Bull. Seism. Soc. Am. 793, 774–789.
Lin, F.-C., Moschetti, M.P., Ritzwoller, M.H., 2008. Surface wave tomography of the western United States from ambient seismic noise: Rayleigh and Love wave phase velocity maps. Geophys. J. Int. 173, 281–298, doi:10.1111/j1365-246X.2008.03720.x.
Malcolm, A.E., Scales, J.A., Van Tiggelen, B.A., 2004. Extracting the Green's function from diffuse, equipartitioned waves. Phys. Rev. E 70, 015601.
Metha, K., Snieder, R., Calvert, R., Sheiman, J., 2008. Acquisition geometry requirements for generating virtual-source data. Leading Edge 27, 620–629.
Nakahara, H., 2006. A systematic study of theoretical relations between spatial correlation and Green's function in one-, two- and three-dimensional random scalar wavefields. Geophys. J. Int. 167, 1097–1105.
Pedersen, H.A., Krüger, F., the SVEKALAPKO Seismic Tomography Working Group, 2007. Influence of the seismic noise characteristics on noise correlations in the Baltic shield. Geophys. J. Int. 168, 197–210.
Paul, A., Campillo, M., Margerin, L., Larose, E., Derode, A., 2005. Empirical synthesis of time-asymmetrical Green's functions from the correlation of coda waves. J. Geophys. Res. 110, B08302, doi:10.1029/2004JB003521.
Roux, P., Sabra, K.G., Kuperman, W.A., Roux, A., 2005. Ambient noise cross correlation in free space: theoretical approach. J. Acoust. Soc. Am. 117 (1), 79–84.
Sánchez-Sesma, F.J., Pérez-Ruiz, J.A., Luz'on, F., Campillo, M., Rodriguez-Castellanos, A., 2008. Diffuse fields in dynamic elasticity. Wave Motion 45 (5), 641–654.
Sato, H., Fehler, M., 1998. Seismic Wave Propagation and Scattering in the Heterogeneous Earth. American Institute of Physics Press.
Scales, J.A., Malcolm, A.E., Van Tiggelen, B.A., 2004. Estimating scattering strength from the transition to equipartitioning. In: AGU Fall Meeting Abstracts, p. B1053.
Shapiro, N.M., Campillo, M., Stehly, L., Ritzwoller, M.H., 2005. High-resolution surface-wave tomography from ambient seismic noise. Science 307 (5715), 1615–1618.
Shapiro, N.M., Campillo, 2004. Emergence of broadband Rayleigh waves from correlations of the ambient seismic noise. Geophys. Res. Lett. 31, L07614, doi:10.1029/2004GL019491.
Snieder, R., 2004. Extracting the Green's function from the correlation of coda waves: a derivation based on stationary phase. Phys. Rev. E 69, 046610.
Stehly, L., Campillo, M., Shapiro, N.M., 2006. A study of the seismic noise from its long-range correlation properties. J. Geophys. Res. 111, B10306, doi:10.1029/2005JB004237.
Van Tiggelen, B.A., 2003. Green's function retrieval and time-reversal in a disordered world. Phys. Rev. Lett. 91, 243904.
Wapenaar, K., 2004. Retrieving the elastodynamic Green's function of an arbitrary inhomogeneous medium by cross correlation. Phys. Rev. Lett. 93, 254301.
Wapenaar, K., 2006. Green's function retrieval by cross-correlation in case of one-sided illumination. Geophys. Res. Lett. 33, L19304, doi:10.1029/2006GL027747.
Weaver, R., Lobkis, O.I., 2004. Diffuse fields in open systems and the emergence of the Green's function. J. Acoust. Soc. Am. 116, 2731–2734.
Weaver, R., Lobkis, O.I., 2005. Fluctuations in diffuse field-field correlations and the emergence of the Green's function in open systems. J. Acoust. Soc. Am. 117 (6), 3432–3439.
Willis, M.E., Lu, R., Campman, X., Toksöz, M.N., Zhang, Y., De Hoop, M., 2006. A novel application of time reverse acoustics: salt dome flank imaging using walk away VSP surveys. Geophysics 71 (2), A7–A11.
Yang, Y., Ritzwoller, M.H., Levshin, A.L., Shapiro, N.M., 2007. Ambient noise Rayleigh wave tomography across Europe. Geophys. J. Int. 168, 259–274.
Yang, Y., Ritzwoller, M.H., 2008. Characteristics of ambient seismic noise as a source for surface wave tomography. Geochem. Geophys. Geosyst. 9, doi:10.1029/2007GC001814.
Yao, H., Van der Hilst, R.D., De Hoop, M.V., 2006. Surface-wave array tomography in SE Tibet from ambient seismic noise and two-station analysis. I. Phase velocity maps. Geophys. J. Int. 166, 732–744.
Yao, H., Beghein, C., Van der Hilst, R.D., 2008. Surface-wave array tomography in SE Tibet from ambient seismic noise and two-station analysis. II. Crustal and upper mantle structure. Geophys. J. Int. 173, 205–219.
Yao, H., Van der Hilst, R.D., 2009. Analysis of ambient noise energy distribution and phase velocity bias in ambient noise tomography, with application to SE Tibet, Geophys. J. Int., doi:10.1111/j.1365-246X.2009.04329.x.